



# Quantitative X-ray computed tomography: Prospects for detailed *in-situ* imaging in bench-scale fire measurements

Emeric Boigné<sup>a,\*</sup>, N. Robert Bennett<sup>b</sup>, Adam Wang<sup>b</sup>, Matthias Ihme<sup>a</sup>

<sup>a</sup> Department of Mechanical Engineering, Stanford University, Stanford, CA, 94305, United States

<sup>b</sup> Department of Radiology, Stanford University, Stanford, CA, 94305, United States

## ARTICLE INFO

### Keywords:

Pyrolysis  
Smoldering  
Wildfires  
X-ray computed tomography  
Bench-scale experiments  
Quantitative measurements

## ABSTRACT

This paper examines how X-ray Computed Tomography (XCT) can provide detailed and quantitative *in-situ* measurements in bench-scale fire experiments. The method is illustrated by employing a tabletop X-ray system to image the combustion of different biomass samples heated by convection and radiation. The XCT measurements are utilized to evaluate the gas temperature and quantify the burning rates. In particular, quantitative measurements of the pyrolysis and char oxidation rates are obtained for different types of biomass. Simultaneous 3D gas temperature measurements are enabled by doping the flow with Kr, an inert X-ray contrast gas. To assess the capabilities of XCT as a quantitative and non-intrusive measurement technique, the accuracy of the method is evaluated through repeatability studies, whereas the invasive impact of the XCT method on the combustion is characterized experimentally and theoretically. Finally, the adsorption of Kr on the char during cooling is evidenced, and its impact on the measurements is discussed. This analysis highlights that the XCT solid measurements are entirely non-intrusive and are repeatable within 5% uncertainties, while using Kr for gas temperature measurements results in only a 15% lower heat transfer by natural convection.

## 1. Introduction

Laboratory fire experiments are widely used to certify flammability requirements, examine fire dynamics, and create reference test data [1–6]. Such measurements provide a characterization of the composition, thermochemical properties, and reaction rates of solid fuels [7,8]. Several commercially available instruments are commonly employed to acquire reference data [9,10], including thermo-gravimetry analyzers (TGA), differential thermal analyzers (DTA), and differential scanning calorimeters (DSC). Radiative heaters such as cone calorimeters are also used in bench-scale experiments, notably to evaluate heat release rates [11–13]. Several research apparatuses have been developed to examine material pyrolysis and fire dynamics under well-controlled conditions. For instance, the Controlled Atmosphere Pyrolysis Apparatus (CAPA) has been employed to acquire pyrolysis data [14,15]. To validate detailed combustion models, burning rates were measured for different materials using the FM Global Fire Propagation Apparatus [13,16,17]. At NIST, the ignition from firebrand showers was investigated with bench-scale tests on the Lofting and Ignition Research (LAIR) facility [18], and at larger scale in the NIST dragon facility [19]. Bench-scale tests have also been performed to investigate novel flame-retardant

materials [20] and fire extinguishing solutions [21].

In bench-scale experiments, thermocouples, scales, and gas analyzers are commonly employed to provide measurements of pointwise temperature, overall mass loss, emissions, and heat release rate. Heat release rate is arguably the most important variable in fire hazards [11], and the oxygen consumption method is frequently used to determine it from the smoke composition, as specified in standard procedures such as ISO 5660-1 or ASTM E1354 [5,11–13]. Although these rather non-intrusive techniques are affordable, they are limited to probe or global measurements. To obtain more detailed measurements, several imaging techniques have been employed to investigate fire dynamics in multi-dimensional configurations. For instance, cameras can provide measurements of pyrolysis propagation rate, flame heights, and fire spread [3,22]. High-speed cameras have been used to study the impact of water droplets on burning wood surfaces [23], showing that water acts not only as a heat sink, but also prevents the transport of volatile flammable gases to the reaction zone. In addition, laser imaging techniques have been employed to characterize the release of gaseous alkali during pyrolysis via induced fragmentation fluorescence [24], and to measure the effect of fuel type on particle generation via absorption [25]. Infrared imaging has been used to measure the reacting surface temperature and

\* Corresponding author.

E-mail address: [eboigne@stanford.edu](mailto:eboigne@stanford.edu) (E. Boigné).

<https://doi.org/10.1016/j.firesaf.2021.103476>

Received 5 July 2021; Received in revised form 26 September 2021; Accepted 10 October 2021

Available online 14 October 2021

0379-7112/© 2021 Elsevier Ltd. All rights reserved.

image smoldering spread [26,27] and wood ignition [28]. Surface temperature measurements of burning biomass have also been acquired using phosphor thermometry [29].

However, resolving the multiphase dynamics of fire remains challenging, in part because of the formation of smoke and tar and the difficulty in probing the heterogeneous combustion processes within the solid matrix. X-ray Computed Tomography (XCT) was recently demonstrated as *in-situ* diagnostic technique for enabling simultaneous measurements of gas temperature and solid density in biomass smoldering experiments [30]. XCT is a well established imaging technique, commonly used in material and biological sciences, as well as in medical CAT scans to reconstruct the 3D structure of solid samples, bones, or organs. The wide-spread use of these systems makes XCT a widely available, affordable, and easy to operate solution for quantitative measurements of fire dynamics. By diluting the ambient flow with Kr, XCT also simultaneously provides measurements of the gas temperature in combustion systems without optical access [31,32]. The present study aims at further exploring the prospects of using XCT to acquire quantitative multiphase measurements in bench-scale fire experiments. In particular, this article aims to demonstrate how rates of pyrolysis and char oxidation can be simultaneously determined via XCT. To this end, the simultaneous rates of flaming and char oxidation are analyzed *in-situ* for four different materials and at varied oxygen concentrations. In addition, this work also evaluates the repeatability of the method and provides a discussion of the invasive impact of the technique on the combustion and flow physics. A description of the experimental method is provided in Sec. 2. Section 3 presents experimental results, and the capabilities of the XCT technique are discussed in Sec. 4. Section 5 closes the manuscript with the conclusions of this study.

## 2. Experimental methods

### 2.1. X-ray computed tomography

In XCT, a beam of X-ray photons is targeted towards a sample, and a detector captures the photons transmitted through the sample. Using a rotation stage, multiple transmission images are acquired at different view angles of the object. After tomographic reconstruction, XCT provides 3D measurements of the field of linear attenuation  $\mu = \rho\zeta$ , which is the product of the local density  $\rho$  and the energy-averaged mass attenuation coefficient  $\zeta$ . This coefficient is only a function of the atomic composition of the material, and values can be measured for the three phases of interests: unburned biomass material, charred material, and Kr gas-phase.

The gas-phase density measurements were calibrated by experimentally evaluating the attenuation of a flow of 50% Kr at a pressure of 1 bar and a temperature of 300 K [31]. In the solid phase, calibration values for the biomass density  $\rho_b^0$  and mass-attenuation coefficient  $\zeta_b^0$  were obtained from XCT acquisitions acquired in the absence of Kr for each type of material studied. Porosity values for each type of biomass were also obtained by comparing scans with and without Kr before combustion [33]. Similar calibration values were obtained for each type of char by repeating this procedure at the end of pure-pyrolysis experiments acquired in flows without oxygen. These values are reported in a separate study [33], showing that up to 27% density variations were observed across the different materials surveyed.

Because the gas-phase density is significantly smaller than the solid density, segmentation in the attenuation measured via XCT with a global threshold enables separation of the two phases [30]. Note that in the gas mixtures considered, only Kr attenuates the X-rays sufficiently to provide a measurable absorption [31]. In this work, a 50% Kr dilution per volume is employed to achieve sufficient signal-to-noise ratio in the gas-phase density measurements. The density measurement in the gas-phase is used to determine the 3D temperature field by assuming an ideal gas, a homogeneous Kr concentration, and an isobaric system

[30–32]. Uncertainties in the temperature measurements were estimated to about 15% at 2000 K and 2% at 300 K. These uncertainties were evaluated from a previous study in which the same XCT system was employed to measure the gas temperature of laminar premixed flames [31]. Besides, the impact of the released gaseous pyrolyzate on the gas-phase measurements by dilution of the Kr flow was neglected, as it was evaluated to result in a reduction of only 3% in the Kr volume fraction [33].

In contrast, inside the solid sample, both the solid material and the Kr atoms localized within the material pores contribute to the attenuation. To isolate the contribution of the solid material only, the attenuation from the gaseous Kr within the fuel pores was estimated by using the solid porosity values measured by calibration, assuming a homogeneous Kr concentration equal to the free-stream value and a gas-temperature determined by thermocouple reading. By subtracting this attenuation from the inner-pore Kr atoms, the solid attenuation term was isolated, thus yielding measurements of the solid density field  $\rho_s$ . Therefore, the XCT acquisitions can be used to provide simultaneous measurements of the 3D field of solid density of the sample imaged, and its surrounding gas-phase temperature [30,31]. For further details on the method, the reader is referred to a separate study [33].

### 2.2. Experimental setup and acquisition method

A bench-scale combustion apparatus was operated inside a laboratory XCT scanner, as shown in Fig. 1. The scanner consists of a X-ray source, a rotation stage on which the experimental apparatus is placed, and a X-ray detector. This XCT system was used in previous studies [30–32]. The experimental apparatus consists of a vertical quartz tube of 57 mm inner diameter in which a mixture of Kr, N<sub>2</sub>, and O<sub>2</sub> is flown at a constant flow rate of  $2.89 \pm 0.12$  L per minute. The Kr concentration is kept at 50% per volume, while the ratio of N<sub>2</sub> and O<sub>2</sub> is varied to achieve O<sub>2</sub> concentrations ranging from 0 to 21% per volume. Cubic samples of 1.6 cm size of different biomass materials are instrumented at the center of the tube, with the grain orientation parallel to the vertical flow. A K-type thermocouple is press-fit into a center hole at the upper surface of each sample, holding them 34 mm above a flat coil heater. The coil heater provides a radiation of about 5.23 kW/m<sup>2</sup> at the lower surface of the sample [33]. A load cell measuring the total mass-loss of the sample is used to validate the X-ray density measurements [30].

To measure the solid density and gas temperature *in-situ*, successive XCT scans were acquired during combustion of the biomass samples. The flow and radiant heater were first stabilized, and at time  $t = 00:00$ , the sample was placed inside the quartz tube. Between 13 and 15 scans were acquired over the 16-min duration of each experiment. At time 16:00, the radiant heater was turned off and an additional 3–5 scans were acquired to image the cooling phase of the burned sample. Each scan consists of 225 projection images acquired during the 360° rotation of the apparatus. The 2048 × 1536 images were acquired at a rate of 7.5 fps, with an exposure time of 40 ms per image. The detector pixel size is 194 μm, while the temporal resolution of about 90 s corresponds to the time delay between two scans. Note that the buoyant flow dynamics of the diffusion flame around the sample are not resolved. In fact, the 3D density and temperature measurements correspond to the temporal average over the 30-s duration of each scan acquisition. In the solid phase, a consumption rate of 0.4 g/min corresponds to a vertical displacement of the reaction front over about 10 voxels during one scan. Therefore, a broadening of the reaction fronts is expected in both the gas and solid phases.

### 2.3. Global combustion kinetics of biomass

To analyze biomass combustion using XCT, a simplified framework describing the global chemical kinetics is considered. To this end, the biomass combustion is modeled as a three-reaction process involving (I) endothermic pyrolysis, (II) exothermic char oxidation or smoldering,

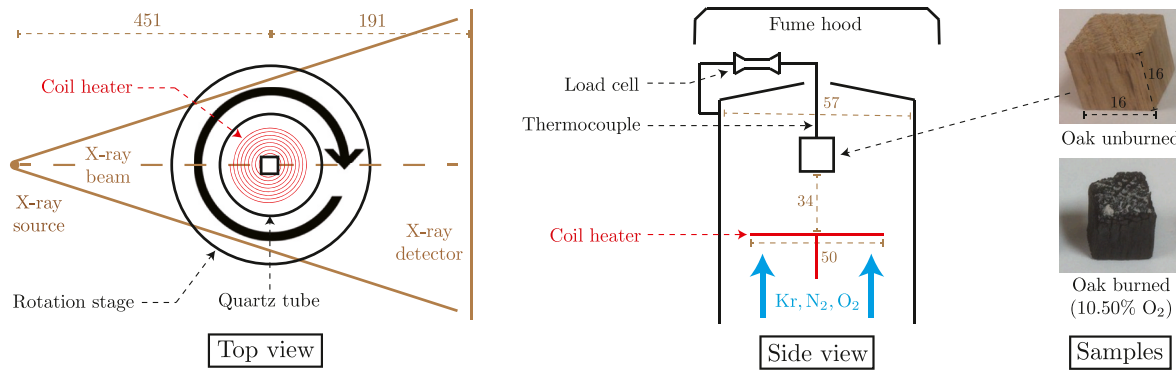
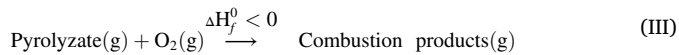
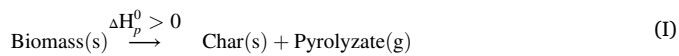


Fig. 1. Schematic of the X-ray system, experimental apparatus, and oak samples with dimensions in mm.

and (III) gas-phase oxidation or flaming. The corresponding reactions are written as [10]:



This mechanism is adequate to describe the global combustion dynamics that are experimentally observed in this work. Specifically, when 1 kg of biomass is pyrolyzed via reaction (I), it yields a mass of  $\nu_c^0$  kg of char and  $\nu_p^0$  kg of volatile pyrolyzate gases, where the volatile content  $\nu_p^0 = 1 - \nu_c^0$  is determined from pyrolysis experiments in an inert flow without oxygen [33].

#### 2.4. Measuring pyrolysis and smoldering reaction rates

When only measuring the total mass of a solid sample undergoing combustion, it is impossible to differentiate between the mass loss due to pyrolysis and the mass loss due to char oxidation. As a result, global load measurements cannot determine the individual contributions from the pyrolysis and the char oxidation. In contrast, XCT can simultaneously measure the total solid volume  $V_s$  and infer the averaged solid density  $\bar{\rho}_s$ . The total solid volume is computed by counting solid voxels, while the averaged density is obtained by integrating over the sample volume the solid density field obtained as described in Sec. 2.1. Using these two independent measurements, it is therefore possible to decouple the mass-loss contributions due to pyrolysis and smoldering. To achieve this, the averaged char volume fraction  $\bar{X}_c$  is first evaluated as

$$\bar{X}_c = \frac{\rho_b^0 - \bar{\rho}_s}{\rho_b^0 - \rho_c^0} \quad (1)$$

in which  $\rho_b^0$  is the unburned biomass density, and  $\rho_c^0$  is the char density, both obtained from calibration for each type of biomass material. The separate volumes of biomass  $V_b = (1 - \bar{X}_c)V_s$  and char  $V_c = \bar{X}_c V_s$  are then computed. Note that the volume fraction of ash is therefore neglected, even though its attenuation contribution is accounted for in the calibrated mass-attenuation coefficients of char and biomass. This approach is validated by results from proximate analysis, indicating that ash account for less than 1% of the mass of the unburned materials [33]. As the pyrolysis reaction (I) is the only reaction consuming biomass, the mass rate of pyrolysis in units of kg of pyrolyzate gases generated per second is directly given by

$$\dot{m}_p = -\nu_p^0 \dot{m}_b = -\nu_p^0 \rho_b^0 \frac{dV_b}{dt} \quad (2)$$

In contrast, the mass balance of char involves both its formation by the pyrolysis reaction (I) and its consumption by oxidation as per reaction (II). Therefore, the char oxidation rate in units of kg of char consumed per second is expressed as

$$\dot{m}_o = -\left(1 - \nu_p^0\right) \rho_b^0 \frac{dV_b}{dt} - \rho_c^0 \frac{dV_c}{dt} \quad (3)$$

In this work, the mass rates of pyrolysis  $\dot{m}_p$  and smoldering  $\dot{m}_o$  obtained from the XCT results using Eqs. (2) and (3) are reported for different operating conditions. Note that in the present formulation, the variations in the char mass  $\frac{dm_c}{dt}$  are approximated as  $\rho_c^0 \frac{dV_c}{dt}$ , meaning that only the mass losses due to surface ablation are attributed to char oxidation. Any variations in the density field within the sample volume are attributed to the pyrolysis through Eq. (1), even if these changes could be due to oxidation within the sample. However, as described in Sec. 3.2.3, the limited variations observed within the density field after pyrolysis suggest that this assumption is reasonable for the conditions studied. In the few complete-pyrolysis cases where the mean density  $\bar{\rho}_s$  reached values slightly below  $\rho_c^0$ , the mean char volume fraction  $\bar{X}_c$  was clipped to 1. In addition, changes in density due to thermal expansion are neglected in this work, but these could compromise solid-phase measurements. However, the largest volume variations due to thermal expansion remained lower than 2%, which were measured for char samples cooling back to ambient temperature once the radiant heater was turned off.

The measurements of pyrolysis and char oxidation rates could be used to estimate the heat release rate contributions from reactions (I) and (II), given proper calibration of the heats of combustion. Specifically, the total heat release rate  $\dot{Q}$  can be expressed as the sum of the positive contributions  $\dot{Q}_f$  and  $\dot{Q}_s$  from the flaming and smoldering reactions, and the negative contribution  $\dot{Q}_p$  from the pyrolysis reaction:

$$\dot{Q} = \dot{Q}_f + \dot{Q}_o + \dot{Q}_p = \dot{Q}_f + \dot{m}_o \Delta H_o^0 + \dot{m}_p \Delta H_p^0 \quad (4)$$

With *a priori* calibration at the conditions investigated, the two last terms on the right-hand side could thus be inferred from XCT measurements. Besides, the XCT measurements of the gas temperature could also be used to construct a global heat balance. Therefore, an energy balance that includes the radiation terms could be derived to evaluate the total heat release rate, as done in the oxygen consumption method [5,11–13]. This approach would have the benefit of separating the three individual heat contributions from the pyrolysis, smoldering, and flaming reactions.

### 3. Results

#### 3.1. 3D measurements of gas temperature and solid density

Fig. 2 presents cross sections of gas temperature and solid density

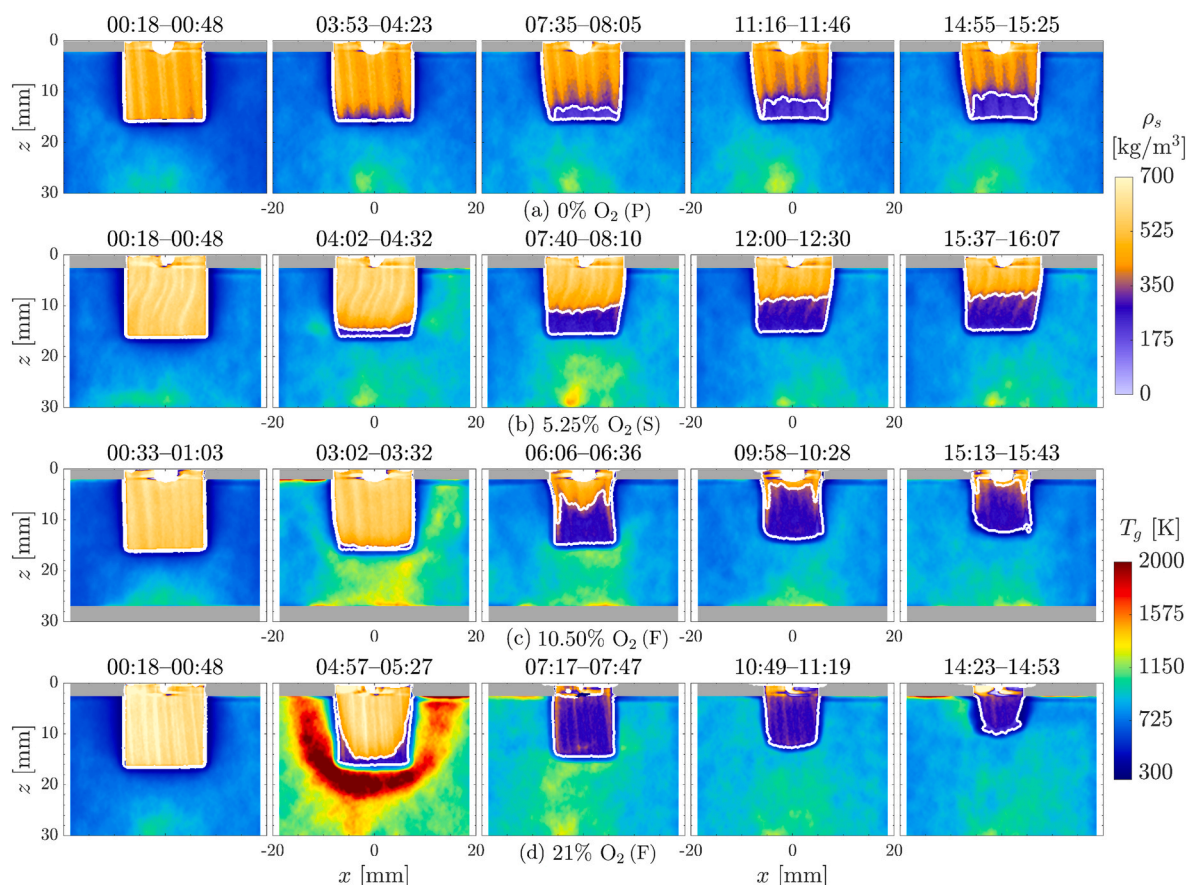


**Fig. 2.** XCT measurements showing vertical cross sections at  $y = 0$  of gas temperature and solid density for birch with oxygen contents of (a) 0%, (b) 5.25%, (c) 10.50%, and (d) 21% per volume. White contours indicate the pyrolysis front.

measured for birch biomass with oxygen concentrations ranging from 0 to 21% per volume. For the 0% oxygen concentration, the solid density results highlight that an internal pyrolysis propagated within the sample, whereas the gas-phase temperature remained unchanged. For the case  $X_{O_2} = 5.25\%$ , a faster pyrolysis propagation was observed, with low rates of smoldering and a slightly higher gas temperature. For the remaining cases with oxygen contents above 10%, gas-phase ignition and subsequent flaming were visually observed. At 10.50%  $O_2$ , ignition was seen at 05:10 with an intermittent flame that extinguished at 07:10. Comparing the results between 5.25 and 10.50% oxygen showed that higher rates of pyrolysis were achieved when additional heat was released by gas-phase combustion. Besides, the recess of the lower surface by smoldering was clearly visible after flaming for the case with 10.50%  $O_2$ . At 21%  $O_2$ , intense flaming was observed, starting at 04:30 and ending at 07:35. The heat release by combustion in the gas-phase enhanced the char conversion, before extinction once the pyrolysis was complete and no more flammable gases were released from the pyrolysis. Because of the intense char oxidation after flaming, layers of ash formed around the sample. The ash locally attenuated the X-ray and thus appears as a low-temperature region in Fig. 2d.

### 3.2. Measurements of solid temperature, pyrolysis, and oxidation rates

As described in Sec. 2.4, XCT enables decoupled measurements of the mass losses due to pyrolysis and char oxidation. Fig. 3 reports temporal profiles of pyrolysis and oxidation rates determined from XCT measurements, along with thermocouple measurements for different operating conditions. Four materials were considered with a vertical grain orientation, parallel to the flow direction. For birch, both parallel and perpendicular grain orientations were studied. Depending on the oxygen

concentration, material type, and grain orientation, different combustion regimes were observed. The pyrolysis (P) regime indicate cases for which the measured char oxidation rate remained below 0.01 g/min. Smoldering (S) corresponds to cases where char oxidation rates above 0.01 g/min were measured, but no flaming was observed. In flaming (F) regimes, gas-phase ignition was visually observed through the transparent quartz tube. For all materials and combustion regimes, the expected monotonic increase of solid temperature, pyrolysis, and oxidation rates with increasing  $O_2$  concentration was retrieved in Fig. 3.

#### 3.2.1. Thermocouple measurements

By examining the thermocouple measurements for the cases with flaming, a sharp change in slope was observed due to the increased heat release after gas-phase ignition. The temperature peaked at the point of maximum flaming intensity, before decreasing as flaming weakened and finally extinguished. In contrast, for conditions belonging to the pyrolysis and smoldering regimes, the thermocouple temperature increased continuously until the heater was turned off at  $16:00 \pm 01:00$ . Overall, once accounting for the varying combustion regimes, the thermocouple measurements were comparable for the different materials considered. However, minor variations in the flaming ignition times were visible from the thermocouple measurements. These variations were explained by the 5% deviations in initial sample mass. In particular, faster heating and ignition correlated with slightly lighter samples, while heavier samples had slightly delayed ignitions.

Only the perpendicular grain condition with flaming birch featured a significantly different temperature profile, with a varying flaming intensity and delayed peak temperature. When the grain was perpendicular to the flow, the flame base attached to the sides of the sample, whereas it would anchor below the sample when the grain was aligned



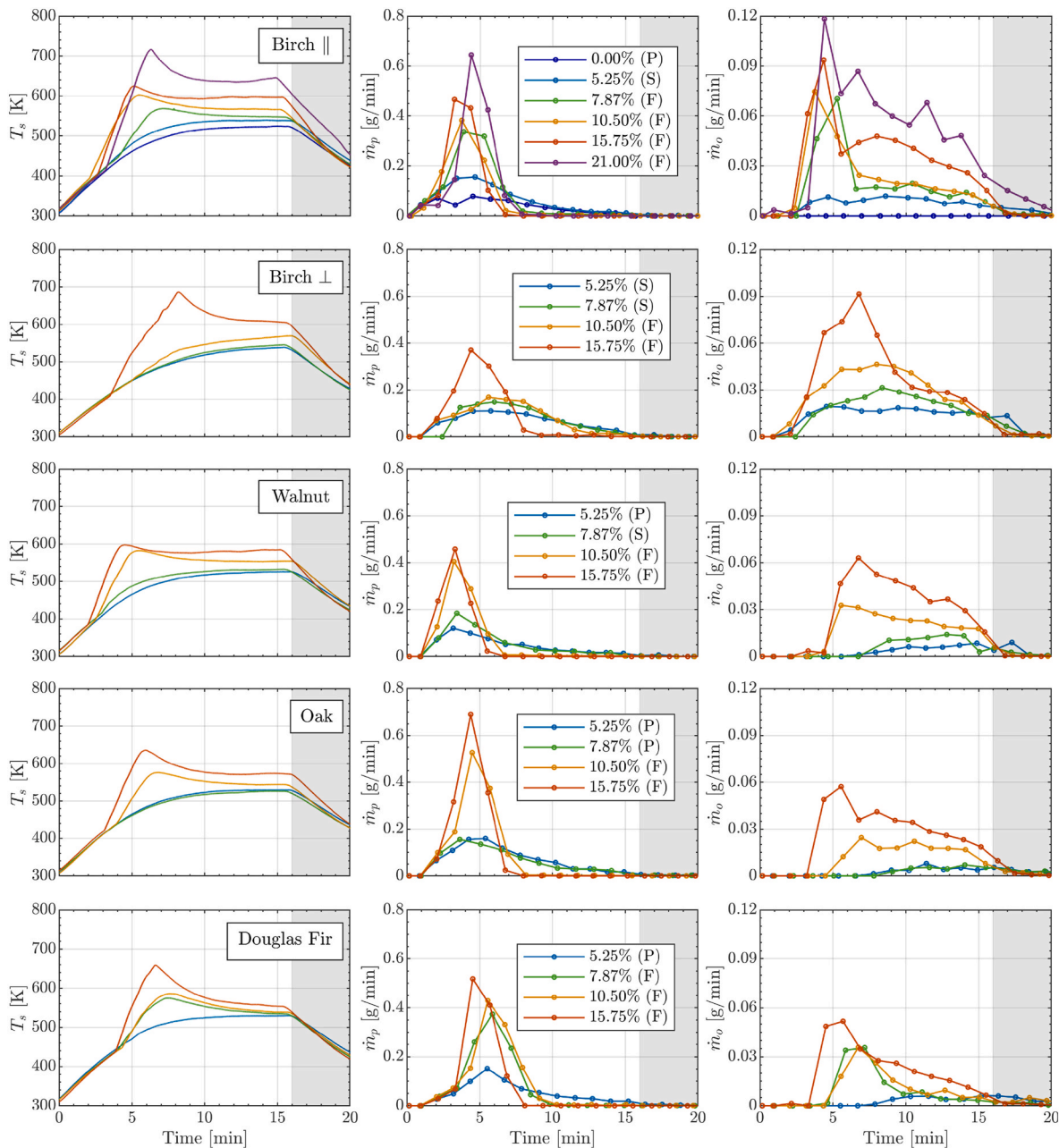


**Fig. 3.** Temporal evolution of (left) thermocouple temperature and X-ray measurements of (center) pyrolysis rates and (right) oxidations rates for different types of biomass. The grain orientation is parallel to the flow, except for birch for which it is either parallel (||) or perpendicular (⊥). Each data point for the rates is constructed by comparing two successive X-ray acquisitions. In the legends, both the  $O_2$  concentration in the flow and the combustion regime are indicated: (P) pyrolysis, (S) smoldering, or (F) flaming.

with the flow. This difference in the flaming mode explained the large differences reported in the thermocouple readings. Besides, comparing smoldering conditions at 5.25%  $O_2$  with perpendicular and parallel grain for birch highlighted that higher temperature measurements are observed with the parallel grain orientation. This result correlated with the higher heat conductivity of wood along the grain, up to twice the value measured across the grain [9].

For birch with parallel grain, a higher temperature was measured for the smoldering case at 5.25%  $O_2$ , compared to the pyrolysis case without oxygen. This increase was explained by the larger heat release due to char oxidation. A similar increase in temperature was observed with walnut for pyrolysis conditions with 5.25%  $O_2$  and smoldering at 7.87%  $O_2$ . However, in this case, the char oxidation rate was zero before 6:00, and smoldering failed to explain the temperature increase. Instead, the

exothermic formation of oxidative pyrolyzate, not decoupled from the thermal pyrolyzate here, could explain this result [34].

### 3.2.2. Pyrolysis rate measurements

Across all conditions, the pyrolysis rates peaked at minute 3–6 of the experiment. Slightly higher pyrolysis rates were observed with smoldering compared to pyrolysis conditions, whereas significantly higher rates were measured for all flaming cases. For the flaming cases, the samples charred entirely within the first 10 min, after which the pyrolysis rates dropped to zero. Comparing the pyrolysis rate measurements across different materials, there was a direct correlation between higher pyrolysis rates and larger solid temperature values. In particular, slight variations in pyrolysis rates were captured, as was well illustrated by the results for walnut at 5.25 and 7.87%  $O_2$ , featuring only a 20 K

difference in solid temperature. Besides, for flaming cases with complete pyrolysis, the time at which the pyrolysis rate dropped to zero was a good indicator of the time of flame extinction.

### 3.2.3. Oxidation rate measurements

Comparing the oxidation rates for the different materials after flaming showed that constant solid temperatures may not directly correlate with constant smoldering rates. In fact, even though the thermocouple reading remained constant, the solid temperature at the smoldering front locally decreased, especially as the surface recessed and moved further away from the radiant heat source.

The measurements of oxidation rate can be used to determine whether heat is simultaneously released from the solid and gas oxidation. During flaming, gaseous oxygen was consumed while heat was released, thus increasing the char and gas temperatures at the surface. This temperature increase tended to enhance the rate of oxidation through smoldering, whereas the reduced amount of O<sub>2</sub> tended to inhibit smoldering. Therefore, there was a competition for O<sub>2</sub> between the two oxidation reactions, making it challenging to assess which reaction dominated, especially in the poorly ventilated configuration investigated here. The simultaneous flaming and smoldering is indicated in Fig. 3 by measurements of significant oxidation before the pyrolysis was completed and the flaming terminated. Simultaneous oxidation was thus observed for Douglas fir and birch. In contrast, for oak, and even more clearly for walnut, there was no or only a limited amount of char oxidation occurring during the flaming phase. With these materials, the heat release was either dominated by gas-phase oxidation or heterogeneous char oxidation.

The competition between heat release by flaming and char oxidation is best illustrated in Fig. 3 with the birch measurements comparing the parallel and perpendicular grain orientations. For the perpendicular grain orientation, the flame was anchored on the sides of the sample, and O<sub>2</sub> was available at the lower surface of the sample where large smoldering rates were achieved during flaming [33]. Furthermore, because the flames were localized downstream of the smoldering front for this case, the oxygen available at the flame location was limited compared to the amount available at the smoldering front. These dynamics explained the significant amount of char oxidation measured during flaming for birch cases with perpendicular grain orientation. In contrast, with the parallel grain orientation, results from Fig. 2 showed that the flame anchored right below the bottom surface of the sample where smoldering occurred. However, significant amounts of char oxidation were still measured during flaming, despite the limited amount of O<sub>2</sub> penetrating through the flame front. In fact, the buoyant flow around the sample was unsteady, and even though the sample was fully engulfed by the flame, the flame fluctuated around that position, allowing O<sub>2</sub> to reach the high-temperature char surface. The XCT measurements were averaged over 30-s periods, and were thus not able to capture these dynamics that occurred at times on the order of 1 s.

As described in Sec. 2.4, the char oxidation rate measurements only accounted for the mass losses by ablation at the smoldering surface. To discuss this assumption, Fig. 4 presents profiles of density measured by XCT at different times for an oak sample operated at 15.75% oxygen. The large density-changes due to pyrolysis were apparent when comparing the first three time-profiles. However, after flaming ended at time 7:00, significant ablation of the char was measured at the smoldering surface, while only minor density changes were measured within the sample volume. These minor changes are indicated by a black arrow in Fig. 4. As per Eq. (1), they were interpreted as mass losses due to further pyrolysis of incompletely transformed biomass driven by the smoldering heat. However, note that it is unclear whether these changes were actually due to pyrolysis or in-depth char oxidation. Because they would represent less than 5% of the mass losses due to ablation, neglecting them in the oxidation rate calculations remained a reasonable assumption. The fact that char oxidation was mainly observed near the smoldering surface can be explained by the limited availability of

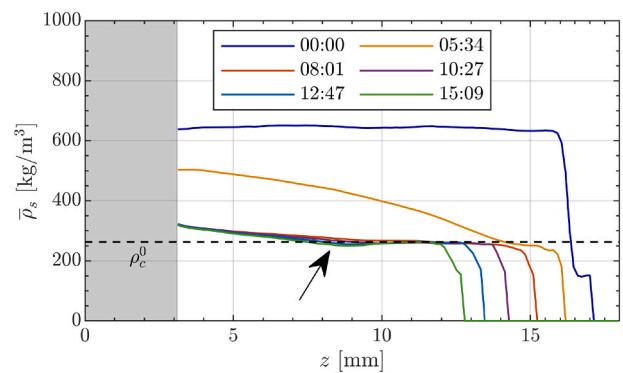


Fig. 4. Profiles of cross-sectional averages  $\bar{\rho}_s$  of the solid density over time for oak at 15.75% O<sub>2</sub>. The dashed line indicates the calibrated char density  $\rho_c^0 = 263 \text{ kg/m}^3$  for oak. The first 3 mm at the top of the sample are greyed-out because of X-ray artifacts originated from the metallic thermocouple tip.

oxygen deep within the sample, especially when the grain was aligned to the vertical flow. Besides, characteristic ember red-glow was visually observed on the lower smoldering surface during the experiments. This visible radiation suggested surface temperature reaching 900–1000 K, whereas thermocouple readings of only 600 K were recorded at the top of the sample. These values indicated strong temperature gradients across the height of the sample, and therefore reduced temperature away from the smoldering surface to drive the char oxidation.

### 3.3. Repeatability of the experiments and influence of Kr

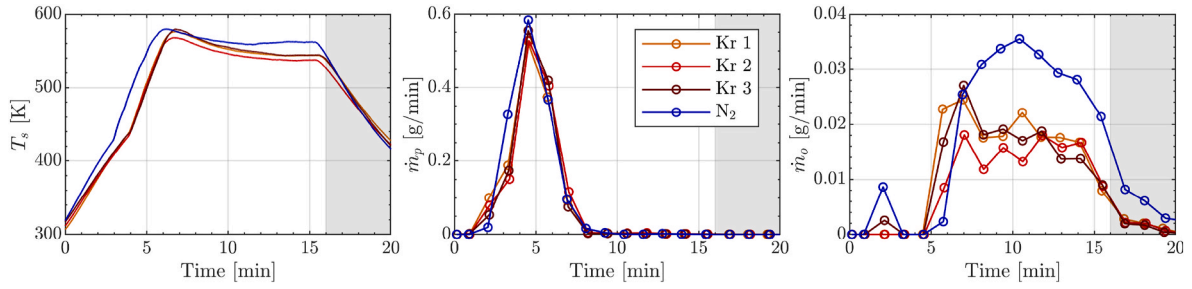
To assess the experimental repeatability and quantify measurement uncertainties, we repeated measurements for one operating condition at 10.50% O<sub>2</sub>. This study was done using oak samples with initial mass of 2.46, 2.47, and 2.49 g, for which flaming regimes were observed. Oak was chosen as it presented the largest irregularities in grain structures among all the materials considered. In the experiments reported so far, a fast acquisition rate was prioritized to the detriment of temporal repeatability of each acquisition. For this specific analysis, successive CT acquisitions were instead started as repeatedly as possible for all runs. Specifically, the time delay between each triplet of scans from the three runs remained lower than 9 s.

Fig. 5 presents the temporal evolution of thermocouple temperature and XCT measurements of pyrolysis and oxidation rates for these three runs. The horizontal cross-section averages of the linear attenuation  $\mu$  were reported for the first eight scans of each run in Fig. 6. The remaining scans were not shown, since only minor changes in attenuation were observed. The comparison of results for these cases provided a quantification of experimental variability. Specifically, only minor discrepancies were observed in thermocouple temperature, pyrolysis rates, and linear attenuation profiles. The largest difference was observed in the oxidation rates, although it remained below  $\pm 0.01 \text{ g/min}$ . Note that this condition was on the lower range of oxidation rates compared to the other conditions reported in Fig. 3, and errors of the order of 0.01 g/min remain small.

Figs. 5 and 6 also include results for a condition acquired by replacing Kr with N<sub>2</sub>. For the two different flow mixtures, flaming was observed. The results highlight that replacing N<sub>2</sub> with Kr only had a limited impact on the combustion. The later ignition and slightly lower oxidation rates observed experimentally with Kr were explained by the reduction in heating by natural convection, primarily due to the lower thermal conductivity of Kr. This point is further analyzed in Sec. 4.2.

## 4. Discussion of X-ray diagnostic method

In this section, the X-ray diagnostic method for quantitative *in-situ* combustion measurements of biomass is further discussed. Specifically,



**Fig. 5.** Temporal evolution of (left) thermocouple temperature, and X-ray measurements of (center) pyrolysis and (right) oxidation rates comparing three identical runs with Kr and one run with N<sub>2</sub>, all acquired at 10.50% O<sub>2</sub> with oak samples.

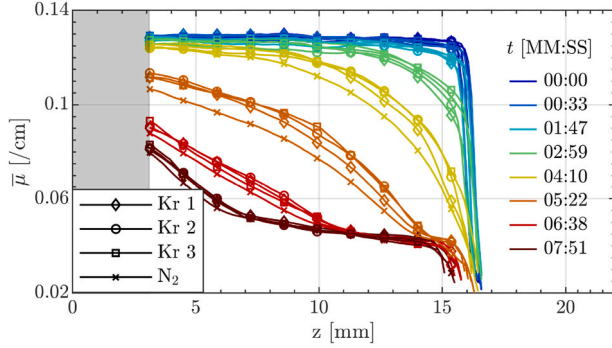


**Fig. 6.** Profiles of cross-sectional averages  $\bar{\mu}$  of the linear attenuation  $\mu$  over time for four repeated runs at 10.50% O<sub>2</sub> with oak: three runs in identical Kr flow, and one with N<sub>2</sub> instead of Kr. The first 3 mm at the top of the sample are greyed-out because of X-ray artifacts originated from the metallic thermocouple tip.

the intrusive impact of XCT with Kr dilution on the flow and combustion physics is analyzed. To this end, we theoretically and experimentally examine the effects of the X-ray absorption and the replacement of N<sub>2</sub> by Kr. The adsorption of Kr onto the char observed post-combustion during cooling is also discussed.

#### 4.1. Influence of X-ray photons on combustion physics

The impact of directing X-ray photons on the sample consists in the accumulation of interaction events between photons and electrons of solid biomass and gaseous Kr atoms. These isolated events may leave the atoms in ionized or excited states, that can trigger fluorescence or heating. However, because the number of X-ray photons is significantly smaller than the number of solid and gaseous atoms considered, only a tiny fraction of atoms will interact with X-ray photons. Specifically, using spectral modeling tools, the photon fluence for the present configuration is computed to about  $3.4 \times 10^{12}$  photons per steradian per second [35]. This estimation was obtained for a tube voltage of 60 kV, a 7 mm Al-equivalent filtration, and a tube current of 23 mA [30]. The flux of X-ray photons corresponding to one detector pixel is thus of the order of  $3 \times 10^5$  photons per second, or a power of  $2 \times 10^{-9}$  W. This number is to be compared with the collision frequency of gas molecules of about  $10^{24}$  collisions per second inside each voxel. It is therefore concluded that the interaction of X-ray photons with the biomass and Kr atoms does not have any significant influence on the combustion process, and XCT in itself is entirely non-invasive. Even with photon flux  $10^9$  times higher, as characteristic of bending magnets used in synchrotron tomography beamlines [36], the impact of the X-ray remains limited.

#### 4.2. Influence of Kr dilution on combustion physics

Replacing N<sub>2</sub> in the gas phase with Kr to measure the gas

temperature changes the thermodynamic properties of the flow. The influence of Kr dilution on the gas phase combustion has been further detailed in a previous study [31], and the present analysis focuses on the impact of Kr on the heat transfer to the solid. To evaluate the impact of Kr dilution on burning rates, another experiment was performed without any Kr in the flow, as reported in Sec. 3.3. The N<sub>2</sub>/O<sub>2</sub> mixture used is compared to the Kr/O<sub>2</sub> mixture in Table 1. This comparison highlights that replacing N<sub>2</sub> with 50% Kr increases the molecular weight and density, and decreases the kinematic viscosity, heat capacity, thermal conductivity and diffusivity. Note that these properties differ only by a few percent when the oxygen concentration is varied from 0 to 21%. The flow velocity was kept constant to preserve the flow rate of oxygen to the sample.

The experimental results from Fig. 5 show that gas-phase ignition occurred about a minute earlier with N<sub>2</sub>, and was followed by a stronger oxidation with slightly higher solid temperatures, but a comparable rate of pyrolysis. At the conditions considered, the cooler sample is heated in a hot flow dominantly by natural convection and radiation, and forced convection can be neglected. Indeed, the Richardson number for the thermal mixing, given by

$$Ri = \frac{gL}{V^2} \frac{T_\infty - T_s}{T_f}, \quad (5)$$

is on the order of 200 for both flows. This value was computed with a flow velocity  $V$  of 1.9 cm/s, a characteristic lengthscale  $L$  of 1.6 cm, a free-stream flow temperature  $T_\infty$  of 950 K, a solid temperature  $T_s$  of 600 K, and a film temperature  $T_f$  given by  $T_f = (T_\infty + T_s)/2 = 775$  K. The temperature values were determined from XCT measurements and thermocouple reading. Because the heating by radiation is the same for both flows, the primary difference is the intensity of the heat transport

**Table 1**

Comparison of the thermodynamic properties at ambient pressure and film temperature  $T_f$  of 775 K for flow mixtures of N<sub>2</sub>/O<sub>2</sub> and Kr/O<sub>2</sub>. The following values were used to compute the non-dimensional numbers: a flow velocity  $V$  of 1.90 cm/s, a characteristic length-scale  $L$  of 1.60 cm, a quiescent flow temperature  $T_\infty$  of 950 K, and a solid temperature of  $T_s = 600$  K.

Flow conditions	N <sub>2</sub> /O <sub>2</sub>	Kr/O <sub>2</sub>
O <sub>2</sub> mole fraction $X_{O_2}$ [%]	10.5	10.5
N <sub>2</sub> mole fraction $X_{N_2}$ [%]	89.5	39.5
Kr mole fraction $X_{Kr}$ [%]	0.0	50.0
Mean molecular weight [g/mol]	28.4	56.3
Density $\rho$ [g/m <sup>3</sup> ]	447	886
Heat capacity $c_p$ [J/kgK]	1106	466
Thermal conductivity $\lambda$ [W/mK]	$5.61 \cdot 10^{-2}$	$3.43 \cdot 10^{-2}$
Thermal diffusivity $\alpha$ [m <sup>2</sup> /s]	$11.3 \cdot 10^{-5}$	$8.32 \cdot 10^{-5}$
Kinematic viscosity $\nu$ [m <sup>2</sup> /s]	$7.98 \cdot 10^{-5}$	$5.51 \cdot 10^{-5}$
O <sub>2</sub> diffusivity $D_{O_2}$ [m <sup>2</sup> /s]	$10.5 \cdot 10^{-5}$	$9.53 \cdot 10^{-5}$
Prandtl number $Pr = \nu/\alpha$	0.70	0.66
Reynolds number $Re = VL/\nu$	3.81	5.52
Richardson number $Ri$	196	196
Rayleigh number $Ra$	2005	3961



by natural convection.

The convective heat transfer from the flow of quiescent temperature  $T_\infty$  to the sample of temperature  $T_s$  is proportional to the temperature difference and to the convective heat transfer coefficient  $h$  of the flow, which is related to the Nusselt number via

$$\text{Nu} = \frac{hL}{\lambda}, \quad (6)$$

where  $\lambda$  is the thermal conductivity of the flow. In flows driven by natural convection, the Nusselt number is commonly determined from empirical correlations as [37]

$$\text{Nu} = f(\text{Pr})\text{Ra}^n, \quad (7)$$

involving an empirical function  $f(\text{Pr})$  of the Prandtl number  $\text{Pr}$ , and a power dependence to the Rayleigh number  $\text{Ra}$ , with  $1/5 \leq n \leq 1/4$  for laminar flows. For an ideal gas the Rayleigh number is defined as

$$\text{Ra} = \frac{gL^3}{\nu\alpha} \frac{T_\infty - T_s}{T_f}, \quad (8)$$

where the kinematic viscosity  $\nu$  and thermal diffusivity  $\alpha$  are evaluated at the film temperature  $T_f$ . Rayleigh values for both flow mixtures are below  $10^6$ . The thermal boundary layer thus remains laminar and Eq. (7) can be used [37]. As reported in Table 1, the Rayleigh number is larger by a factor of two for the Kr flow. However, because of the weak power dependence, Kr dilution results in a Nusselt number only 20% higher. Instead, a larger difference in  $h$  comes from the 40% reduction in the heat conductivity for the Kr flow. The heat transfer rate from the flow to the sample is therefore higher without Kr in the flow, thereby explaining the earlier ignition and higher oxidation rates observed experimentally.

Note that the oxidation rate is a function of the transport of both heat and oxygen. The oxygen transport can be characterized using an oxygen-specific Richardson number, emphasizing that natural convection also dominates forced convection. Because both mixtures have similar mixture-averaged diffusivities  $D_{O_2}$ , the transport of  $O_2$  is therefore comparable in both cases. Therefore, despite the relatively important changes in flow properties between the  $N_2/O_2$  and  $Kr/O_2$  mixtures, it is concluded that the impact of using Kr on the combustion physics remains limited.

#### 4.3. Kr adsorption onto cold char

Finally, the adsorption of Kr onto the carbon-activated char is discussed. After the heater was turned off at time 16:00, the sample cooled down in a flow of 50% Kr and an increase in attenuation  $\mu$  was measured within the sample, near the lower surface. This added attenuation exceeded the amount expected from the gaseous Kr atoms located within the solid matrix pores. It was therefore concluded that additional Kr was stored within the char material via adsorption. Note that adsorption was only observed at ambient temperature, and therefore does not affect previous measurements. Indeed, adsorption is an exothermic reaction, and the thermodynamic equilibrium predicts that less adsorption occurs at higher temperature [38,39]. In the remainder of this section, the Kr adsorption observed during the cooling phase is quantified. The results indicate that Kr adsorption could be used to provide further characterization of the char sample *a posteriori*, including measurements of specific surface area and permeability.

The adsorption of Kr onto different substrates, including shale rocks, coal, and biochar is well understood [38–45]. Kr adsorption consists primarily of physisorption, which is well characterized with the Lennard-Jones potential constant, the polarizability, and the van der Waals radii. The values of these properties differ by only 5% between Kr and  $CH_4$ , indicating that these two gases will similarly adsorb [41]. As a result, studies of the adsorption of  $CH_4$  onto coal [42,45], or cellulose and lignin [44], can be used to understand the adsorption of Kr onto charred materials. One study suggests adsorption of the order of 0.2

mmol of  $CH_4$  per gram of charred substrate at ambient conditions [44], a value comparable to what is measured here.

In the present experiments, Kr atoms within the solid char are either gaseous atoms located within the solid pores, or atoms adsorbed onto the char surface. The storage, defined as the ratio of the stored Kr density  $\rho_{Kr}$  to the Kr gas density outside the solid  $\rho_{Kr}^0$  is written as [41].

$$S = \frac{\rho_{Kr}}{\rho_{Kr}^0} = \varepsilon_s + \frac{\rho_{Kr}^{ad}}{\rho_{Kr}^0} = \frac{\Delta\mu}{\mu_{Kr}^0}, \quad (9)$$

in which  $\varepsilon_s$  is the solid porosity,  $\rho_{Kr}^{ad}$  is the density of adsorbed Kr, and the last equality relates the storage to measurable X-ray quantities: the difference in attenuation  $\Delta\mu$  comparing scans with and without Kr within the char, and the ambient gas-phase attenuation  $\mu_{Kr}^0$  of Kr. Because adsorption occurs at specific sites along the surface of the substrate, the adsorption amount is often expressed on a mole-specific basis, over the mass of substrate [42,45].

$$q_{Kr} [\text{mol/g}] = \frac{1}{M_{Kr}} \frac{\rho_{Kr}^{ad}}{\rho_c^0} = \frac{1}{M_{Kr}} \frac{\rho_{Kr}^0}{\rho_c^0} (S - \varepsilon_s), \quad (10)$$

in which  $q_{Kr}$  is called the loading or uptake of Kr,  $M_{Kr}$  is the molecular weight of Kr.

Fig. 7 presents spatial profiles of storage  $S$  and loading  $q_{Kr}$  measured along the vertical  $z$ -direction for different birch samples after cooling. These measurements were acquired using a first scan with Kr started once the thermocouple reading reached 310 K, and a second scan without Kr taken after flushing the tube with air for 2 min. The storage and loading were then computed using Eqs. (9) and (10) from cross-section averages of  $\mu$ . At a concentration of 0% oxygen, the biomass sample had not charred significantly, and the least amount of adsorption was measured. With oxygen concentrations of 5.25, 7.87, and 15.75%, the storage peaked at a value of  $S = 2.5$ , far exceeding the porosity contribution of 0.5–0.8. The decay of the adsorption along the  $z$ -axis is likely due to the slow diffusion of Kr within the biochar pores, which can take hours to equilibrate [40,43].

## 5. Conclusions

This work investigated the capabilities of X-ray Computed Tomography (XCT) to provide quantitative *in-situ* measurements of both the solid and gas phases in bench-scale fire experiments. The XCT solid measurements were used to infer the rates of pyrolysis and char oxidation, and evaluate when smoldering occur. Specifically, comparisons between different materials highlighted that concurrent heat release by smoldering and flaming only occur for certain types of biomass, and largely depends upon grain orientation. In addition, uncertainties in the solid XCT measurements were shown to remain below 5% through

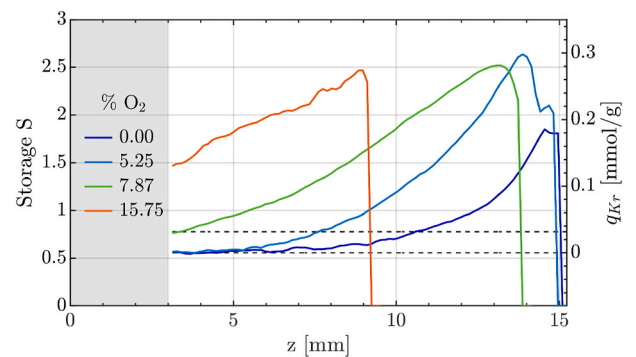


Fig. 7. Profiles of Kr storage  $S$  and loading  $q_{Kr}$  along the height  $z$  for parallel-grain birch at different oxygen concentrations. Results were computed from cross-section averages of  $\mu$ . The two horizontal dashed lines indicate the mean biomass and char values of porosity for birch on the storage axis.



repeatability studies, while the intrusive nature of the diagnostic method on the combustion dynamics was examined. This analysis supports that XCT in itself has negligible impact on the combustion physics, and that the 3D solid density measurements are entirely non-invasive. In contrast, the Kr dilution required to simultaneously measure the 3D gas temperature affects the heterogeneous combustion. However, through experimental and theoretical analysis, it was shown that even a 50% Kr dilution only slightly alters the burning rates. Indeed, the buoyant laminar flow regime was preserved, and the Kr dilution only induced a 15% decrease in sample heating by natural convection. Therefore, XCT is demonstrated as a robust diagnostic method for quantitative *in-situ* measurements with only limited invasive impact to image bench-scale fire experiments.

In the context of fire imaging, XCT offers several opportunities. First, XCT has been extensively used in medical, biological and material sciences, and a versatile range of XCT systems are therefore both readily available and affordable to operate. XCT systems thus represent a relatively low-cost solution for material characterization and quantitative *in-situ* measurements for fire experiments. Second, the capabilities of XCT to resolve *in-situ* the 3D multiphase dynamics of heterogeneous combustion are unique, thereby making it a promising technique to provide detailed quantitative datasets important for model development and validation. In particular, the temporal resolution in this study was limited to 30 s to achieve sufficient photon counts to enable Kr temperature measurements. However, faster solid-phase dynamics could be resolved by performing only the solid-phase measurements over shorter scan durations. Third, with proper calibration, XCT measurements could estimate the heat contributions due to pyrolysis and char oxidation. By complementing the oxygen consumption method used to determine global heat release rates [5,11–13], XCT could also be employed for *in-situ* evaluation of the heat release due to flaming. This combined approach would enable the detailed spatio-temporal characterization of the heat release contributions due to pyrolysis, char oxidation, and flaming. Fourth, the 3D solid measurements enable the detailed analysis of several processes, including the 3D volume shrinkage from pyrolysis [33,46,47], the interaction between chemistry and thermomechanical stress [48], as well as the fire suppression from fire retardants [49]. Fifth, the field of view of modern laboratory X-ray scanners is relatively large, thus providing the ability to image even larger systems, such as entire logs or parts of a tree [50]. Inversely, at the micrometer scale, high-resolution synchrotron sources could be used to analyze the transport of hot O<sub>2</sub> gases within solid micro-pores. Finally, the 3D solid surface obtained by XCT could enable the *in-situ* reconstruction of the solid surface temperature simultaneously measured with an infrared camera. Combining XCT and infrared imaging could therefore provide further detailed reference datasets with solid density, gas, and surface temperature measurements.

#### CRedit authorship contribution statement

**Emeric Boigné:** Conceptualization, Investigation, Methodology, Visualization, Writing – original draft. **N. Robert Bennett:** Investigation, Resources. **Adam Wang:** Resources, Supervision. **Matthias Ihme:** Conceptualization, Resources, Supervision, Writing – review & editing.

#### Declaration of competing interest

The authors declare that they have no known competing financial interests or personal relationships that could have appeared to influence the work reported in this paper.

#### Acknowledgments

This work was supported by NSF with Award No. CBET-1800906 and FM Global.

#### References

- [1] D. Duthinh, K. McGrattan, A. Khaskia, Recent advances in fire-structure analysis, *Fire Saf. J.* 43 (2008) 161–167.
- [2] N. Ren, J. de Vries, X. Zhou, M. Chaos, K.V. Meredith, Y. Wang, Large-scale fire suppression modeling of corrugated cardboard boxes on wood pallets in rack-storage configurations, *Fire Saf. J.* 91 (2017) 695–704.
- [3] L. Jiang, C.H. Miller, M.J. Gollner, J.H. Sun, Sample width and thickness effects on horizontal flame spread over a thin PMMA surface, *Proc. Combust. Inst.* 36 (2017) 2987–2994.
- [4] C.M. Lannon, S.I. Stoliarov, J.M. Lord, I.T. Leventon, A methodology for predicting and comparing the full-scale fire performance of similar materials based on small-scale testing, *Fire Mater.* 42 (2018) 710–724.
- [5] D. Zeinali, S. Verstockt, T. Beji, G. Maragkos, J. Degroote, B. Merci, Experimental study of corner fires—Part I: inert panel tests, *Combust. Flame* 189 (2018) 472–490.
- [6] S. Chan Kim, K.Y. Lee, A. Hamins, Energy balance in medium-scale methanol, ethanol, and acetone pool fires, *Fire Saf. J.* 107 (2019) 44–53.
- [7] C. Lautenberger, G. Rein, C. Fernandez-Pello, The application of a genetic algorithm to estimate material properties for fire modeling from bench-scale fire test data, *Fire Saf. J.* 41 (2006) 204–214.
- [8] Z. Ghorbani, R. Webster, M. Lázaro, A. Trouvé, Limitations in the predictive capability of pyrolysis models based on a calibrated semi-empirical approach, *Fire Saf. J.* 61 (2013) 274–288.
- [9] S. Hostikka, A. Matala, Pyrolysis model for predicting the heat release rate of birch wood, *Combust. Sci. Technol.* 189 (2017) 1373–1393.
- [10] F. Richter, A. Atreya, P. Kotsovinos, G. Rein, The effect of chemical composition on the charring of wood across scales, *Proc. Combust. Inst.* 37 (2019) 4053–4061.
- [11] V. Babrauskas, D.R. Peacock, Heat release rate: the single most important parameter in fire hazard, *Fire Saf. J.* 18 (1992) 255–272.
- [12] P. Boulet, G. Parent, Z. Acem, T. Rogaume, T. Fateh, J. Zaida, F. Richard, Characterization of the radiative exchanges when using a cone calorimeter for the study of the plywood pyrolysis, *Fire Saf. J.* 51 (2012) 53–60.
- [13] J.C. Thomas, R.M. Hadden, A. Simeoni, Experimental investigation of the impact of oxygen flux on the burning dynamics of forest fuel beds, *Fire Saf. J.* 91 (2017) 855–863.
- [14] J. Li, J. Gong, S.I. Stoliarov, Gasification experiments for pyrolysis model parameterization and validation, *Int. J. Heat Mass Tran.* 77 (2014) 738–744.
- [15] J.D. Swann, Y. Ding, M.B. McKinnon, S.I. Stoliarov, Controlled atmosphere pyrolysis apparatus II (CAPA II): a new tool for analysis of pyrolysis of charring and intumescent polymers, *Fire Saf. J.* 91 (2017) 130–139.
- [16] C.F. Schemel, A. Simeoni, H. Biteau, J.D. Rivera, J.L. Torero, A calorimetric study of wildland fuels, *Exp. Therm. Fluid Sci.* 32 (2008) 1381–1389.
- [17] M. El Houssami, A. Lamorlette, D. Morvan, R.M. Hadden, A. Simeoni, Framework for submodel improvement in wildfire modeling, *Combust. Flame* 190 (2018) 12–24.
- [18] S.L. Manzello, S. Suzuki, The new and improved NIST Dragon's LAIR (Lofting and Ignition Research) facility, *Fire Mater.* 36 (2012) 623–635.
- [19] S.L. Manzello, S. Suzuki, Experimentally simulating wind driven firebrand showers in wildland-urban interface (WUI) fires: overview of the NIST firebrand generator (NIST dragon) technology, *Procedia Eng.* 62 (2013) 91–102.
- [20] T. Gong, Q. Xie, X. Huang, Fire behaviors of flame-retardant cables part I: decomposition, swelling and spontaneous ignition, *Fire Saf. J.* 95 (2018) 113–121.
- [21] B. Mykhalichko, H. Lavrenyuk, O. Mykhalichko, New water-based fire extinguishant: elaboration, bench-scale tests, and flame extinguishment efficiency determination by cupric chloride aqueous solutions, *Fire Saf. J.* 105 (2019) 188–195.
- [22] M.A. Finney, J.D. Cohen, J.M. Forthofer, S.S. McAllister, M.J. Gollner, D. J. Gorham, K. Saito, N.K. Akafuah, B.A. Adam, J.D. English, R.E. Dickinson, Role of buoyant flame dynamics in wildfire spread, *Proc. Natl. Acad. Sci. Unit. States Am.* 112 (2015) 9833–9838.
- [23] A. Albadi, Y. Zhang, Experimental study of water droplet impact on burning wood surfaces, *Proc. Combust. Inst.* 38 (2021) 4605–4613.
- [24] C. Erbel, M. Mayerhofer, P. Monkhouse, M. Gaderer, H. Splithoff, Continuous in situ measurements of alkali species in the gasification of biomass, *Proc. Combust. Inst.* 34 (2013) 2331–2338.
- [25] J.G. Radney, R. You, M.R. Zachariah, C.D. Zangmeister, Direct in situ mass specific absorption spectra of biomass burning particles generated from smoldering hard and softwoods, *Environ. Sci. Technol.* 51 (2017) 5622–5629.
- [26] B.D. Smucker, T.C. Mulky, D.A. Cowan, K.E. Niemeyer, D.L. Blunck, Effects of fuel content and density on the smoldering characteristics of cellulose and hemicellulose, *Proc. Combust. Inst.* 37 (2019) 4107–4116.
- [27] H.M. Amin, Y. Hu, G. Rein, Spatially resolved horizontal spread in smoldering peat combining infrared and visual diagnostics, *Combust. Flame* 220 (2020) 328–336.
- [28] L. Terrei, Z. Acem, V. Georges, P. Lardet, P. Boulet, G. Parent, Experimental tools applied to ignition study of spruce wood under cone calorimeter, *Fire Saf. J.* 108 (2019) 102845.
- [29] W. Weng, H. Feuk, S. Li, M. Richter, M. Alde, Z. Li, Temporal temperature measurement on burning biomass pellets using phosphor thermometry and two-line atomic fluorescence, *Proc. Combust. Inst.* 38 (2021) 3929–3938.
- [30] E. Boigné, N.R. Bennett, A. Wang, K. Mohri, M. Ihme, Simultaneous in-situ measurements of gas temperature and pyrolysis of biomass smoldering via X-ray computed tomography, *Proc. Combust. Inst.* 38 (2021) 3899–3907.

- [31] E. Boigné, P. Muhunthan, D. Mohaddes, Q. Wang, S. Sobhani, W. Hinshaw, M. Ihme, X-ray computed tomography for flame-structure analysis of laminar premixed flames, *Combust. Flame* 200 (2019) 142–154.
- [32] J. Dunmon, S. Sobhani, M. Wu, R. Fahrig, M. Ihme, An investigation of internal flame structure in porous media combustion via X-ray computed tomography, *Proc. Combust. Inst.* 36 (2017) 4399–4408.
- [33] E. Boigné, N.R. Bennett, A. Wang, M. Ihme, Structural analysis of biomass pyrolysis and oxidation using in-situ X-ray computed tomography, *Combust. Flame* (2021), <https://doi.org/10.1016/j.combustflame.2021.111737>. In press.
- [34] C. Lautenberger, C. Fernandez-Pello, A model for the oxidative pyrolysis of wood, *Combust. Flame* 156 (2009) 1503–1513.
- [35] J. Punnoose, J. Xu, A. Sisniega, W. Zbijewski, J. Siewerdsen, Spektr 3.0—a computational tool for X-ray spectrum modeling and analysis, *Med. Phys.* 43 (2016) 4711–4717.
- [36] S. Mobilio, F. Boscherini, C. Meneghini, *Synchrotron Radiation*, Springer, 2016.
- [37] T.L. Bergman, F.P. Incropera, D.P. DeWitt, A.S. Lavine, *Fundamentals of Heat and Mass Transfer*, John Wiley & Sons, 2011.
- [38] S. Chen, L. Jin, X. Chen, The effect and prediction of temperature on adsorption capability of coal/CH<sub>4</sub>, *Procedia Eng.* 26 (2011) 126–131.
- [39] J. Zou, R. Rezaee, K. Liu, Effect of temperature on methane adsorption in shale gas reservoirs, *Energy Fuel* 31 (2017) 12081–12092.
- [40] D.H. Maylotte, C. Spiro, P.G. Kosky, E.J. Lamby, X-ray Computed Tomography of Coal: Final Report, Technical Report, DOE/MC/19210-2357, US Department of Energy, 1986.
- [41] X.-C. Lu, G.P. Pepin, R.M. Moss, A.T. Watson, Determination of gas storage in devonian shales with x-ray-computed tomography, in: *SPE Annual Technical Conference and Exhibition*, 1992, pp. 455–466.
- [42] X.Q. Liu, X. He, N.X. Qiu, X. Yang, Z.Y. Tian, M.J. Li, Y. Xue, Molecular simulation of CH<sub>4</sub>, CO<sub>2</sub>, H<sub>2</sub>O and N<sub>2</sub> molecules adsorption on heterogeneous surface models of coal, *Appl. Surf. Sci.* 389 (2016) 894–905.
- [43] S. Mayo, M. Josh, D. Kasperczyk, J. Kear, J. Zhang, J. Dautriat, M. Pervukhina, M. B. Clennell, R. Sakurovs, N. Sherwood, A. Maksimenko, C. Hall, Dynamic micro-CT study of gas uptake in coal using Xe, Kr and CO<sub>2</sub>, *Fuel* 212 (2018) 140–150.
- [44] S. Pourebrahimi, M. Kazemeini, M. Zaroudi, H.R. Bozorgzadeh, Methane adsorption on carbonaceous microporous materials prepared from cellulose and lignin: equilibrium and kinetic studies, *Sci. Iran.* 25 (2018) 3368–3380.
- [45] D. Gao, L. Hong, J. Wang, D. Zheng, Molecular simulation of gas adsorption characteristics and diffusion in micropores of lignite, *Fuel* 269 (2020) 117443.
- [46] R. Mooser, F. Forsberg, E. Hack, G. Székely, U. Sennhauser, Estimation of affine transformations directly from tomographic projections in two and three dimensions, *Mach. Vis. Appl.* 24 (2013) 419–434.
- [47] K. Li, S. Hostikka, P. Dai, Y. Li, H. Zhang, J. Ji, Charring shrinkage and cracking of fir during pyrolysis in an inert atmosphere and at different ambient pressures, *Proc. Combust. Inst.* 36 (2017) 3185–3194.
- [48] S. Wang, P. Ding, S. Lin, X. Huang, A. Usmani, Deformation of wood slice in fire: interactions between heterogeneous chemistry and thermomechanical stress, *Proc. Combust. Inst.* 38 (2021) 5081–5090.
- [49] E. Boigné, N.R. Bennett, A. Wang, M. Ihme, Examining the Effect of Fire Retardant on the Combustion of Wood via X-Ray Computed Tomography, 12th U.S. National Combustion Meeting, 2021. Paper 1B13.
- [50] W. Mell, A. Maranghides, R. McDermott, S.L. Manzello, Numerical simulation and experiments of burning douglas fir trees, *Combust. Flame* 156 (2009) 2023–2041.